Investigating the Coherence Bandwidth and Coherence Distance of Radio Signals Scattered from Urban Building Point Clouds Using Physical Optics

Arjen Velkers

***Abstract*—In this paper the coherence bandwidth and coherence distance of radio channel are investigated in a realistic non-line-of-sight urban setting in Helsinki, where the geometrical information of the environment is characterized using point clouds and the scattered radio signals are computed using physical optics with modified equivalent currents. The surface irregularity of a street wall described by deterministic point clouds is also modeled as a stochastic Gaussian process, providing take-aways for other researchers on simulating the measured reality. The computed radio channel is composed of specular reflection and diffuse scattering at lower 5G frequency bands. Coherence in frequency and spatial domains are calculated and analyzed for different polarized pair of antennas at link ends. The values provide take aways for other researchers on how to design the radio systems for site-specific and mission-critical urban scenarios. The results show that: 1) the antenna polarization does not significantly influence the channel coherence due to the non-negligible contribution of diffuse scattering (non-specular) to radio channel; 2) the frequency continuity can still be observed over 3.6 to 7.8 MHz, but the spatial consistency is very bad ranging from 7.0 to 15.5 mm with the contamination of the coherent specular reflection with the non-coherent diffuse scattering.**

***Index Terms*—Radio channel, urban outdoor, specular and diffuse scattering, physical optics, coherence**

I. Introduction

A radio channel is the physical medium where radio signals travel from transmitter to receiver. As radio systems and antennas are designable whilst the real-world environment is uncontrollable, the description and characterization of a radio propagation channel provide insightful information for the optimized design of antennas and systems for site-specific applications. A radio channel is mostly composed of multiple components resulting from the different types of physical mechanism of the radio-environment interactions, namely, the direct line-of-sight (LOS), the specular reflection, the diffraction, the penetration and the diffuse scattering [1]. Given the far-field plane wave assumptions, a multi-component radio channel can be characterized as multipath, where the ”ingredients” of each path include the angle of arrival, the angle of departure, the complex polorimetric gain, the delay and the Doppler spread (if in mobility).

The frequency response of a time-varying multipath channel results in distinct performance metrics over the spatial-temporal evolution, the antenna separation/irregularity and the carrier frequency. The key parameters in spatial and frequency domains include, but not limited to, the coherence bandwidth and coherence distance [2]. The spatial and frequency coherence are used to quantitatively describe the spatial and frequency selective fading that occurs in a channel. The coherence bandwidth is the frequency range over which the CTF holds a certain degree of correlation. The coherence distance is the distance of the antenna separation beyond which the channels associated with the separated antenna locations are no longer correlated. The spatial coherence can provide insight into whether a channel is in fast or slow fading when a certain speed applied to a mobile antenna. The frequency coherence tells whether a channel shows frequency selective fading or flat fading.

Under the context of the intensive standardization and deployment of 5G systems, the spatial and frequency coherence for various scenarios at lower 5G band (sub-6 GHz) [3],[4] and mmWave band [5] have been studied. The urban outdoor is one of the most common communication scenarios, and it is crucial that the radio systems perform in a decent quality in such scenario even when mission-critical, e.g., under non-line-of-sight (NLOS) channel conditions. Limited studies [6] have investigated the spatial and frequency coherence in NLOS urban outdoor scenarios, where the wavelength, even at the lower 5G band, is comparable to the dimension of the urban building surface irregularity and hence diffuse scattering occurs with non-negligible power contribution to the radio channels [7].

Nevertheless, there have not been any paper, to the best of the author’s knowledge, that investigates the correlation properties for a large part of the lower band of the 5G standard, in a scenario where the only pathway of radio signals from transmitter to receiver is via a rough wall in a realistic urban setting. Investigating this NLOS scenario could shed some light on urban radio communications in critical connectivity missions, thus is the goal of this paper. This paper investigates multiple carrier frequency ranges falling in the scope of the lower 5G bands can give insight into the frequency continuity within these bands. Information on the frequency continuity as well as the spatial consistency of the radio channel in aforementioned scenarios provides hint on how to optimally design the site-specific radio systems, especially in regard to the use of modulation schemes like frequency-division multiplexing.

In this paper, to study the spatial and frequency coherence, both the realistic environment wherein the radio signals propagate along and the mechanisms of radio-object interaction will be described and modeled. The geometrical information of an

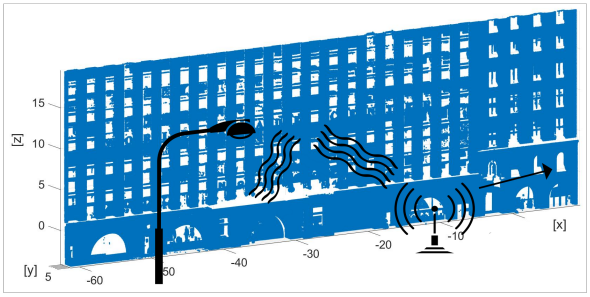

Fig. 1: Raw point clouds in vertical plane along the street

urban street wall is captured by laser scanning as point clouds (a.k.a. the 3D positioning data of objects). The macroscopic irregularity of building surface is deterministically characterized through the facets constructed from the neighbouring points. Roughness profile with parameterization on key influencing factors is further extracted for readers to generate stochastically the measured reality. With the geometrical information including surface roughness, the electromagnetic properties of materials including dielectric and conductivity, as well as the definition of link terminals, the radio channel can be computed and investigated in frequency-spatial domains. In this paper, we use tri-polarized orthogonal dipoles (electric, half-wavelength long) as antennas at link ends, as these dipole modes form the generic fundamental set of arbitrary patterns of antennas. Assuming the absence of LOS, the NLOS paths via the rough wall are mainly composed of specular reflection and diffuse scattering; we name the two mechanism collectively as ”scattering”. The scattering is calculated by physical optics (PO) with modified equivalent current approach (MECA) [8]. The carrier frequencies considered are the 3 GHz, 4 GHz and 5 GHz bands, covering the lower 5G bands providing insight into the realistic scenario of pre-5G NLOS urban street.

The paper is organized as follows. The methodology is explained in section II. In section III the numerical investigation is covered. Finally the paper is concluded in section IV.

II. Methodology

In this section, first we introduce the method on how to capture and characterize the geometrical information (surface irregularity) of a real-world street wall. Second we introduce the radio signal computation method. At last, we illustrate the key parameters extracted from the radio signals for engineering take-aways.

A. Point clouds

When computing the scattering of radio waves from a wall it is important to consider the surface irregularity. Note that the inhomogeneity of wall materials is out of the scope of this paper and we assume that the materials are all with the same dielectric properties. The macroscopic surface irregularity is described as a roughness profile which can be modeled either stochastically or deterministically. In terms of the stochastic modelling, the roughness is commonly modeled as a correlated

Fig. 2: Real-world street view provided by Google Map

Gaussian process [7], [9], whose key parameters are the root mean square (rms) height and the correlation length. The rms height gives an indication of the perpendicular roughness profile as how much the height of the surface deviates from the reference mean of the height. The correlation length tells more about the parallel roughness profile as how fast the surface profile varies over the spread of the surface. With the Rayleigh or the more rigorous Fraunhofer criteria [10], it is possible to determine the degree of roughness of a surface with the rms height, the incident angle and the wavelength.

One the other hand, the surface roughness profile can be acquired deterministically as point clouds [5], from which the stochastic profile mentioned above can also be extracted. The point cloud in this paper is obtained by laser scanning of the Aleksanderinkatu street in the center of Helsinki, Finland. A glance at the real-world street view can be found in Fig. 2, where the main construction materials in the street are tinted window glass and architectural stone. The point clouds were obtained by doing multiple scanning measurements at several locations. The accuracy of the collected points is about 1 mm at the 5 m distance from the laser scanner, and the point cloud density is approximately 0.9 points per cm^2. Since laser scanning has greater uncertainty in capturing transparent objects, the window surfaces are manually filled in afterwards from the captured raw data.

As is shown in Fig. 1, the point cloud was constructed from the laser scanned data, where the captured wall is 85.4 m in length and 28.7 m in height. The reconstruction of a few neighbouring points into a local surface generates a facet. A normal vector is calculated for each of these facets. To make predictions about the channels and furthermore the spatial and frequency coherence, as well as to evaluate the applicability of the scattering computation technique, the roughness profile of the wall surface is characterized from the point cloud and fit to

TABLE I: Roughness profile of the wall

Parameter		Value [cm]
Large scale	rms height	11.14
Small scale	rms height	0.33
	Average side length of facets	1.84
	Average distance between points	2.03
	Correlation length in z-direction	19.75
	Correlation length in x-direction	18.75

the stochastic correlated Gaussian process with key parameters extracted.

Prior to the roughness characterization of the point cloud, the alignment to eradicate the coordinate offset caused by the biased view angles from scanner's positions, as well as the outlier elimination, were implemented. It is worth noting that the global coordinate system follows the coordinate shown in Fig. 1. The length of the wall surface runs in the x direction and the height in the z direction. As can be observed from the Fig. 1, the perpendicular roughness profile, or the rms height, is aligned with the y-axis, whilst the parallel roughness profile, or the coherence length, is aligned with the x-z plane. For characterizing roughness a distinction is made between the large scale and small scale. The large scale roughness tells more about the height variation as a result of the ridges and grooves in the wall. The small scale roughness is taken over the relatively "flat" parts of the wall and gives more useful information for predicting the specular and diffuse scattering. For both the large and small scales the rms height of the surface is computed and shown in Table I. Moreover, the average size of the facet generated with neighbouring points is also computed and shown in the table, giving information about the applicability of the PO method at certain frequencies. In addition, the correlation length of the surface roughness in the x and z direction is also calculated and shown in Table I.

B. Computation of radio signals

1) Physical optics with modified equivalent current: To compute the radio channel composing of scattered multipath, PO with modified equivalent current approach is utilized. PO is an intermediate method between geometrical optics that ignores wave effects, and full wave methods using precise electromagnetic theory. PO gives a good approximation of the electromagnetic fields when applied to high frequency and low curvature scenarios in the lit region. A high frequency approximation method indicates that the surface of an object is much larger compared to the wavelength of impinging waves. The lit region is the region illuminated by sources. PO has wide applicability for scatterers with different shapes and materials. Although it was originally developed for analyzing scattering from perfect electric conductor, the concept of current approximation is general and applicable for dielectric materials and bodies with surface impedance [11]. PO takes less computation time compared to rigorous full wave approaches where the induced currents on a scatterer surface are determined by a large set of linear equations [12], which can be extremely time-consuming. The major source of errors in PO is at the edge of surface, or when the surface curvature is large and multiple reflections occur. This source of errors can be neglected in this paper: as the scale of the captured wall is much larger than the first or second Fresnel zone of Tx/Rx locations, the building corner edge and the other local edge effect are ignored.

The standard process of applying PO-MECA to compute the scattered field and furthermore the channel is as follows. The incident fields impinging on a surface create the equivalent electric and magnetic surface currents. These surface currents act as a source, creating the electric and magnetic fields that radiate away from the surface. The surface should be considered as flat. To account for the fact that the street wall surface in this paper is rough, the surface is divided into smaller local surfaces (a.k.a. facets), whose dimensions are much smaller than the wavelength of the radio signal. These facets are regarded as flat, which means that PO is applicable. The total scattered field in this case is the sum of the contributions from all the relevant facets.

The key equations of the PO with MECA used in this paper are shown as below. The way the incidence field determines the equivalent electric current $\boldsymbol{J}$ and equivalent magnetic current $\boldsymbol{M}$ is depicted below:

$$\begin{aligned}\boldsymbol{J} &= \frac{1}{\eta}\left[\boldsymbol{E}_{\mathrm{TE}}^{\mathrm{inc}}\cos\Theta_{\mathrm{inc}}\left(1-R_{\mathrm{TE}}\right)\hat{\boldsymbol{e}}_{\mathrm{TE}}\right.\\ &\quad\left.+\,\boldsymbol{E}_{\mathrm{TM}}^{\mathrm{inc}}\left(1-R_{\mathrm{TM}}\right)\left(\hat{\boldsymbol{n}}\times\hat{\boldsymbol{e}}_{\mathrm{TE}}\right)\right]|_{\Delta S}\\ \boldsymbol{M} &= \left[\boldsymbol{E}_{\mathrm{TE}}^{\mathrm{inc}}\left(1+R_{\mathrm{TE}}\right)\left(\hat{\boldsymbol{e}}_{\mathrm{TE}}\times\hat{\boldsymbol{n}}\right)\right.\\ &\quad\left.+\,\boldsymbol{E}_{\mathrm{TM}}^{\mathrm{inc}}\cos\Theta_{\mathrm{inc}}\left(1+R_{\mathrm{TM}}\right)\hat{\boldsymbol{e}}_{\mathrm{TE}}\right]|_{\Delta\mathrm{S}}\end{aligned} \tag{1}$$

where $\boldsymbol{E}_{\mathrm{TE}}^{\mathrm{inc}}$ and $\boldsymbol{E}_{\mathrm{TM}}^{\mathrm{inc}}$ are the transverse electric (TE) and the transverse magnetic (TM) components of the incident electric field $\boldsymbol{E}^{\mathrm{inc}}$ respectively, Θ_{inc} is the incident angle to the facet, R_{TE} and R_{TM} are the TE and TM mode reflection coefficients, respectively, $\hat{\boldsymbol{e}}_{\mathrm{TE}}$ denotes the unit vector of the TE mode field, and $\eta = \sqrt{\frac{\mu}{\epsilon - j\frac{\sigma}{\omega}}}$ denotes the impedance of free space where μ is the free space permeability, ϵ is the permittivity, σ is the conductivity, $\omega = 2\pi f$ is the angular frequency and f denotes the frequency. How the narrowband channel is determined by the antenna responses and the scattered field calculated by PO-MECA is shown below:

$$\boldsymbol{H}\left(f\right) = \sum_{l=1}^{L}\boldsymbol{A}_{\mathrm{rx}}\left(\boldsymbol{k},f\right)\boldsymbol{E}^{\mathrm{scat}}\left(\boldsymbol{k},\boldsymbol{\kappa},f\right)\boldsymbol{A}_{\mathrm{tx}}^{T}\left(\boldsymbol{\kappa},f\right) \tag{2}$$

where $\boldsymbol{H} \in \mathbb{C}^{N_{\mathrm{r}}\times N_{\mathrm{t}}}$ is the channel transfer function (CTF) composed of scattered multipath, $\boldsymbol{E}^{\mathrm{scat}} \in \mathbb{C}^{3\times 3}$ is the scattered field as Cartesian vector, $\boldsymbol{A}_{\mathrm{tx}} = [\boldsymbol{a}_{\mathrm{tx},x}, \boldsymbol{a}_{\mathrm{tx},y}, \boldsymbol{a}_{\mathrm{tx},z}] \in \mathbb{C}^{N_{\mathrm{t}}\times 3}$ is the array response of Tx antennas, $\boldsymbol{A}_{\mathrm{rx}} = [\boldsymbol{a}_{\mathrm{rx},x}, \boldsymbol{a}_{\mathrm{rx},y}, \boldsymbol{a}_{\mathrm{rx},z}] \in \mathbb{C}^{N_{\mathrm{r}}\times 3}$ is the array response of Rx antennas, $l = 1,\ldots,L$ is the index for the facet in effective surface area, L is the total facet number, and f denotes the frequency. $\boldsymbol{\kappa} = [x_t, y_t, z_t]$ denotes the unit vector from the Tx location to the facet center, $\boldsymbol{k} = [x_r, y_r, z_r]$ denotes the unit vector from the facet center to the Rx location. N_{t} denotes the number of transmitting antenna polarizations and N_{r} the number of receiving antennas.

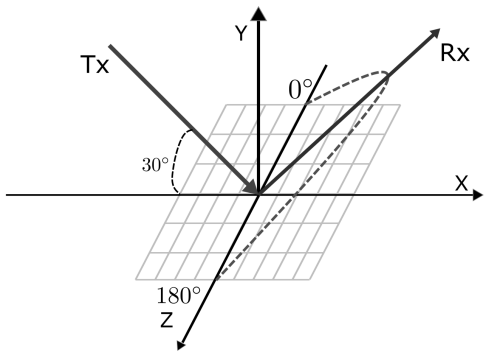

Fig. 3: Simulation setup to test the scattering computation

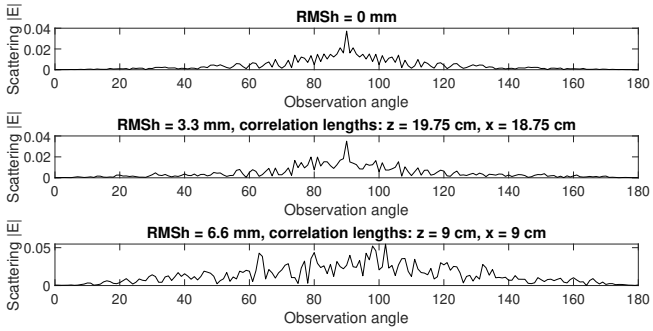

Fig. 4: The scattered power against observation angle for flat and rough surfaces

2) Verification of the computation: The way waves scatter from a surface, depends on the roughness of the surface. The scattered field from a surface with a certain degree of roughness can be described as the combination of a mean and a fluctuating component, where the mean component indicates the contribution of specular reflection from a flat surface and the fluctuation component corresponds to diffuse scattering from surface irregularity [10]. Therefore to validate our code of PO-MECA, scattering is simulated for various roughness profiles in the cut plane specular to the incidence field. As is shown Fig.3, the incident field is in angle of 30° relative to the surface plane, and the observation angles are uniformly sampled in the specular cut plane as the dot line. The size of the surface is 1 m^2 and the observation distance is 10 m or 100λ. In this verification simulation, both Tx and Rx antennas are z-polarized and the center frequency is 3 GHz. As can be seen in Fig. 4, the scattering from the surfaces that are not flat, can be seen as the combination of the reflection from the flat surface with a fluctuating component coming from the roughness of the surface. It can also be observed that the rougher the surface, the bigger the contribution from the fluctuating component. The observations are within the theoretical expectations hence the validity of the code is verified.

C. Coherence bandwidth and coherence distance

For the calculation of the coherence bandwidth, a vast range of narrowband signals with constant spacing in frequency is transmitted over the channel to form a wideband channel. This range should be larger than the expected coherence bandwidth so that the multipath can be resolved for inspection. The wideband CTF $\boldsymbol{H} \in \mathbb{C}^{N_\mathrm{t} \times N_\mathrm{r}}$ is obtained over N_f frequency points for all polarized combinations. The coherence bandwidth can be calculated from $\boldsymbol{H}$ in two ways.

On one hand, the coherence bandwidth can be found by the ACF. By the correlating the ACF of $\boldsymbol{H}$ over all sampled frequencies, ACF coefficients are found as a function of frequency lag. The ACF coefficient of each polarized pair $\{\alpha, \beta\} = \{xx, xy, xz, yx, yy, yz, zx, zy, zz\}$ is normalized by:

$$\rho_m = \frac{\sum_{n_f=1}^{N_f-m} H_{\{\alpha,\beta\}}^{n_f} H_{\{\alpha,\beta\}}^{n_f+m}}{\sum_{n_f=1}^{N_f} H\{\alpha,\beta\}^{n_f} H\{\alpha,\beta\}^{n_f}}, \tag{3}$$

where $n_f = 1, \ldots, N_f$ is the index of the transmitted narrowband signals at the n_f-th frequency sample, and m is the index for the lag. The coherence bandwidth is defined as the lag value multiplying the frequency spacing at which the correlation goes below a certain level. Commonly chosen levels are 1/e, 0.5, 0.7 and 0.9 [13].

The other method for computing the coherence bandwidth is by looking at the delay spread. The delay spread is a measure of the difference in time of arrival of the earliest major path and the delayed paths. The delay spread is in the time domain and related to the impulse response of the channel. The impulse response of the channel can be obtained from the CTF by the inverse Fourier transform. From this impulse response the power delay profile (PDP) can be found. PDP shows the power of the delayed multipath components. From the PDP the mean delay spread and the rms delay spread [14] can be computed. The rms delay spread τ_rms and coherence bandwidth are related where a common relation [14] is given by:

$$B_c = 1/(\alpha \cdot \tau_\mathrm{rms}), \tag{4}$$

where α depends on the shape of PDP and the simulation environment. The delay spread will not be converted to coherence bandwidth in this paper as deriving a value for α is not possible with current simulation setup. In this computation setting, obtaining an empirical value for α can only be achieved by randomly generating the rough wall following the extracted surface profile. Due to time and computing restraints this is out of the scope for this paper, but it is good to be aware that the coherence bandwidth can be derived by using this method, given the appropriate settings.

The coherence distance is calculated from the ACF of transfer functions over a spatial evolution. To obtain the coherence distance, the distance between the Tx and Rx antennas is changed. From the coherence distance it is also straightforward to obtain the coherence time. If the speed of the mobile antenna is known the coherence time is simply the coherence distance divided by the speed.

III. Numerical investigations

A. Acceleration of computation

To speed up PO-MEAC computation in an efficient yet effective manner for the large street wall in Helsinki, the

following strategies are applied. First, the integration of the current densities over the facets is simplified, where the phase distribution over each facet is assumed to be constant. With everything inside the field integral being constant over the facet, everything can be taken outside the integral and the integral just yields the size of the facets. Second, the facets within certain surface area, i.e., only part of the street wall instead of the entire wall captured by point clouds, are used. The minimum yet effective choice of the target wall surface can greatly enhance the runtime and save computation power. To this end, the *effective surface* is proposed to be the part of the wall where most of the occurred scattering can impinge on the receiver. The following is the reasoning to find this effective surface. In the case of specular reflection, the Fresnel zone between the Tx and the mirror source of Rx to the wall is the effective area that specular reflection occurs. By calculating the effective area using reflections for point cloud [15], it yields effective areas that are smaller than the first Fresnel zone. In the case of diffuse scattering co-existing with specular reflection, using the aforementioned effective surface for specular reflection would underestimate the actual field strengths, due to the "diffuse" nature. Therefore the effective area is made larger than the in [15] to incorporate as much ds contribution as possible within the constraints of computing power. The settled value for the effective area will be 5 times the first Fresnel zone.

The center of this spanned version of the effective surface of specular reflection is the intersection line from the source to the mirror image of the receiver over the wall.

B. Simulation specification

The key parameters for simulating the NLOS urban street radio channel propagating via the rough wall are shown in Table II. The frequency bands satisfy 1) the applicability of the PO technique and 2) are also useful common pre-5G bands. One the one hand, the way how radio waves interact with the environment depends largely on frequency. With the increase of frequency, the wavelength becomes smaller and the radio signals "see" (or perceive) the small scale objects as becoming larger. To accurately represent the physical reality, the scale of the facets should be much smaller (in the order of 0.1λ) than the wavelength. This effectively puts an upper limit on the applicable frequency to the point clouds with fixed density. On the other hand, choosing the frequency range falling within the regulated 5G bands makes the simulation scenario relevant. The 5G standard has two frequency ranges, a sub-6 GHz band and a band that goes from 25 GHz to 40GHz or above [16]. The mnWave bands are too high for PO to be applicable to the given point cloud, where the wavelength becomes smaller than the average side length of the locally constructed facet from point cloud. Therefore frequencies in the lower band are used. The simulations are conducted at the 3 GHz, 4 GHz and 5 GHz bands. Correspondingly, the side length of the facets compared to the wavelength is 0.18λ, 0.24λ and 0.31λ at 3 GHz, 4 GHz and 5 GHz respectively. To capture the multipath effect, the wideband channel is simulated sweeping 2000 frequency samples over a bandwidth of 400 MHz.

TABLE II: Simulation Specifications

Parameter	**Value**		
	band 1	band 2	band 3
Center frequency	3 GHz	4 Ghz	5 GHz
Bandwidth	400 MHz		
Tx antenna type	x-, y-, z- oriented half-wavelength dipoles		
Rx antenna type	x-, y-, z- oriented half-wavelength dipoles		
Tx antenna location	x = -50, y = -5, z = 5 [m]		
Rx antenna lications	x = -20.5 to x = -19.5, y = 2.5, z = 2 [m]		

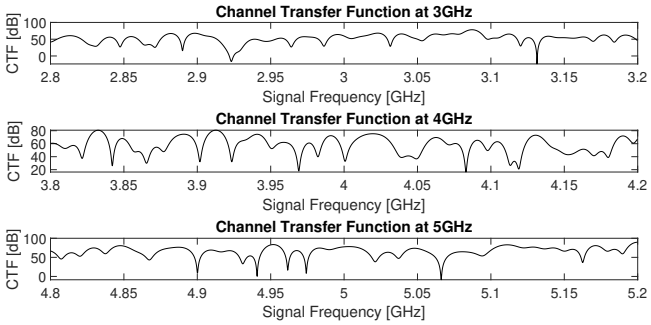

Fig. 5: Channel transfer functions at different signal frequencies at constants Tx-Rx separation of 31.1 m

As can be observed from Table II, there is a height difference of the Tx and Rx antennas. In our scenario, the Tx antenna is assumed to be mounted on a lamp post as a BS antenna and the Rx antenna is assumed to be mobile (either handheld or mounted above a vehicle) as a UE antenna. The simulated radio channel is for downlink. The tri-polarized (orthogonal x-y-z-polarized) half-wavelength electric dipoles are assumed as link ends antennas. The setups of antennas represent a genetic case where the arbitrary antenna patterns can be described as the weighted sum of the fundamental dipole modes. The initial distance between Tx and Rx antennas is set to 30 m. To investigate the coherence distance the Rx antenna moves further away from the Tx antenna in a path parallel to the wall. The distance sweep contains 2000 locations where the Rx antenna moves in a total of 1 m, such that the spatial resolution is decently high.

C. Numerical examples

There are 3×3 polarized pairs of Tx-Rx antennas and mainly the results with z-polarized Tx and Rx are demonstrated here. The readers can find the rest results in the Appendix. Examples of the developments of the CTF amplitudes at the aforementioned frequency bands and spatial samples are plotted in Fig. 5 and 6, respectively. It can be observed that the channel experiences frequency-dependent periodic deep fades. To provide a quantitative insight into the periodicity of these fades, the normalized ACFs of the channel against frequency spread and antenna separation are shown in Fig. 7 and Fig. 8, respectively. From these normalized ACFs, the coherence bandwidths are extracted: $B_{0.9} = 4.8$ MHz, $B_{0.9} = 4.2$ MHz and $B_{0.9} = 4.2$ MHz for 3 GHz, 4

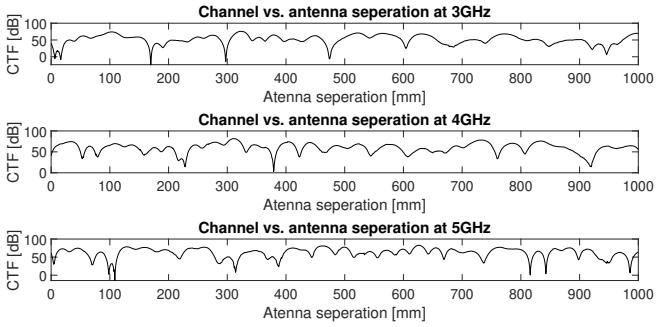

Fig. 6: Channel amplitude vs Tx-Rx separation for different center frequencies

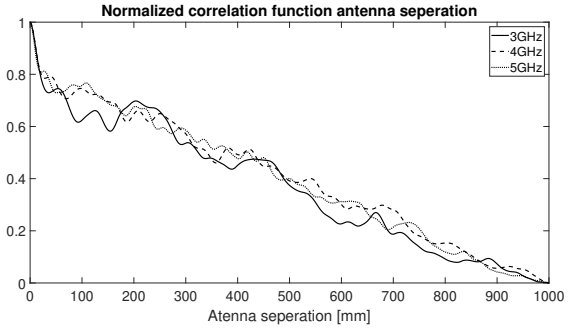

Fig. 8: Normalized correlation function against antenna separation

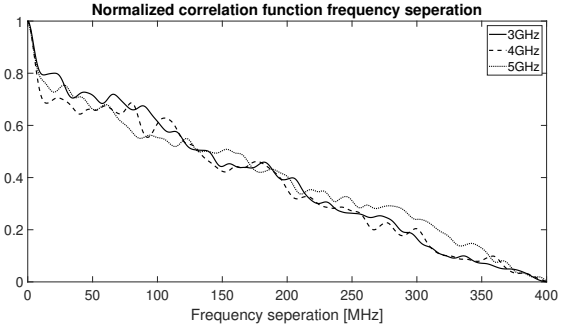

Fig. 7: Normalized correlation function against frequency separation

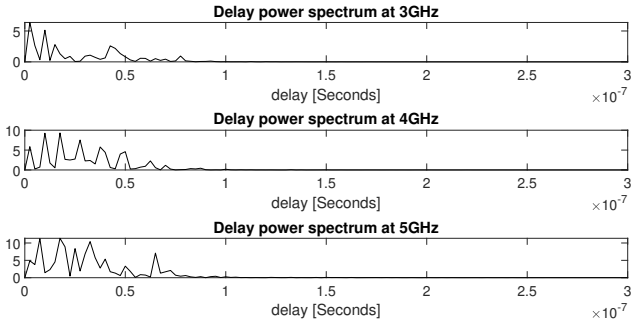

Fig. 9: PDP

GHz and 5 GHz, respectively. Along with this the coherence distances are obtained, yielding: $D_{0.9} = 11$ mm, $D_{0.9} = 11$ mm and $D_{0.9} = 9$ mm. These values are very similar over the 2 GHz gap from 3 GHz to 5 GHz; in other words, the correlation properties don't change over the 3 frequency bands. Furthermore the coherence distances can easily be converted to coherence time by multiplying them with the speed of the mobile antenna. If for example the mobile antenna is assumed to be moving at an average walking speed of 1.5 m/s, the coherence times are: 16.5 ms, 16.5 ms and 13.5 ms for 3 GHz, 4 GHz and 5 GHz. In addition, from CTF the PDP is calculated and shown in Fig. 9. From these PDPs the rms delay spreads τ_{rms} are calculated, giving $\tau_{rms} = 24.7$ ns, $\tau_{rms} = 21.8$ ns and $\tau_{rms} = 42.3$ ns for 3 GHz, 4 GHz and 5 GHz, respectively. Since only the first-order scattering is taken into account the computation, given the fact that the delay resolution is $\frac{1}{400e6} = 2.5$ ns, the numbers of the effective delay bins are roughly 10, 9, 17, respectively. Since the effective surface contributing to the scattering connecting Tx and Rx is limited, the effective delay bin is also limited whereas the rest delay bins fall into the noise floor. The rms delay spreads for all frequencies and all polarized pairs are displayed in Fig 10 at a fixed Tx-Rx separation of 31.6 m. In addition to one particular large value at 5 GHz, there is no significant variations of τ_{rms} over different polarized pairs, which coincides with the case for the coherent bandwidth.

D. Discussion

From the results some observations can be made. Firstly the correlation properties do not seem to depend on the polarizations of the receiving or transmitting antenna. Particularly interesting is the fact that there is no observable difference in correlation properties between co-polarization and cross-polarization. This is likely because of the high diffuse scattering component in the scattered signal. Another observation that can be made is that the correlation properties do not change in a significant way for the considered three frequency bands, pointing frequency continuity in this scenario. The coherence distance is smaller than the considered wavelength, where the spatial consistency is critical and one can expect severe link quality changes over spatial evolution under such NLOS scenarios.

IV. Conclusion

This paper has investigated the frequency-spatial domain coherence of the polarized radio propagation channel in a realistic non-line-of-sight urban setting in Helsinki, Finland. Point clouds were used to encapsulate the geometrical and roughness information of a real-world street wall. Scattering, including both the specular and diffused reflections, was calculated by using physical optics and modified equivalent currents approach. The radio channel was calculated from the scattered field involving the effects of array responses at link ends. From the transfer functions of the computed channels, the coherence bandwidth and coherence distance were analyzed with regard to influencing factors of co- and cross- polarization, frequency continuity, spatial consistency.

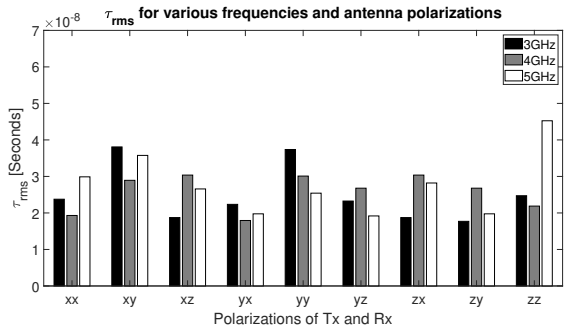

Fig. 10: τ_{rms} for all frequency bands and all polarized pairs of Tx-Rx antennas

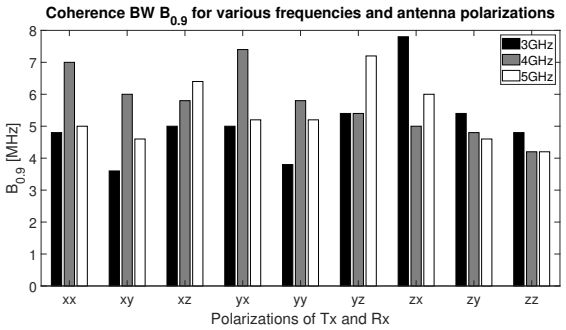

Fig. 11: Coherence Bandwidth $B_{0.9}$ for all frequency bands and all polarized pairs of Tx-Rx antennas

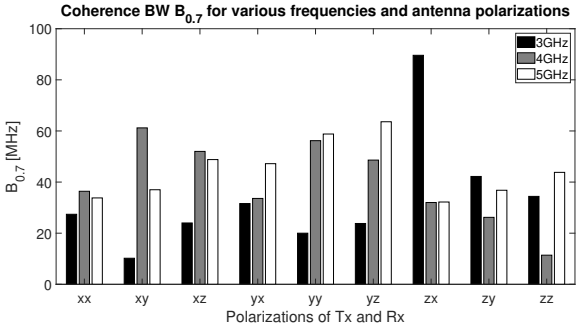

Fig. 12: Coherence Bandwidth $B_{0.7}$ for all frequency bands and all polarized pairs of Tx-Rx antennas

The contributions of this paper are summarized as follows.

- The surface irregularity of the urban street wall captured by the deterministic point clouds is modeled as a correlated Gaussian process, where the parameterization of the process provides valuable take-aways for the readers. One does not need to repeat laser scanning measurements but just using the extracted parameters to emulate the realistic urban street scenario for the purpose of radio system design or simply for its geometrical attribute.
- With carrier frequencies at lower 5G band, under the mission-critical non-line-of-sight scenarios where specular reflection and diffuse scattering contribute to the channel, it is found that the polarization of antennas at link ends does not play a critical role in influencing the channel coherence.
- In terms of coherence, despite of the mix of both specular and diffuse components each with considerable power contribution, frequency continuity can still be expected, but the spatial consistency is very bad due to the contamination of the coherent specular reflection with non-coherent diffuse scattering. The computed coherence bandwidth ranges from 3.6 to 7.8 MHz, and the coherence distance ranges from 7.0 to 15.5 mm where the wavelength range is from 60 to 100 mm.

As future work, the computation efficiency of the code can be further improved to support a virtual walk of the mobile user in large distances with wideband frequency sweeping, to further provide empirical values of coherence distance and bandwidth. Furthermore, the localization of active users in such critical scenarios through the scattered radio multipath is also an interesting direction to go, which combines both communication and sensing at the right time of the commencement of 6G research.

APPENDIX

The appendix tables include Table 11, Table 12, Table 13, Table 14, Table 15, and Table 16.

ACKNOWLEDGMENT

I would like to thank my supervisor Dr. Yang Miao for guiding me through my bachelor assignment and providing me with the large part of the code for calculating the scattering. Furthermore I would like to thank Prof. Katsuyuki Haneda from Aalto Uni. for providing the raw point cloud data, and Mr. Pasi Koivumäki from Aalto Uni. for filling up the window surface in the raw Point cloud data. This work was carried out on the Dutch national e-infrastructure with the support of SURF Cooperative, under the Application Compute Call No. 45550 "Evaluating focusing performance of massive MIMO system in diffuse-scattering-rich environment".

REFERENCES

[1] J.B. Andersen, T.S. Rappaport and S. Yoshida, "Propagation measurements and models for wireless communications channels," in *IEEE Communications Magazine*, vol. 33, no. 1, pp. 42-49, Jan. 1995, doi:10.1109/35.339880.

[2] B. Sklar, "Rayleigh fading channels in mobile digital communication systems .I. Characterization," in *IEEE Communications Magazine*, vol. 35, no. 7, pp. 90-100, July 1997, doi: 10.1109/35.601747.

[3] C. Bergljung and P. Karlsson, "Propagation characteristics for indoor broadband radio access networks in the 5 GHz band," in *Proc. Ninth IEEE International Symposium on Personal, Indoor and Mobile Radio Communications (Cat. No.98TH8361)*, Boston, MA, USA, 1998, pp. 612-616 vol. 2, doi: 10.1109/PIMRC.1998.734312.

[4] W. Debaenst, A. Feys, I. Cuinas, M. Garcia Sanchez, and J. Verhaevert, "RMS delay spread vs. coherence bandwidth from 5G indoor radio channel measurements at 3.5 GHz band," in *SENSORS*, vol. 20, no. 3, 2020, 20, 750.

[5] J. Järveläinen, K. Haneda and A. Karttunen, "Indoor Propagation Channel Simulations at 60 GHz Using Point Cloud Data," in *IEEE Transactions on Antennas and Propagation*, vol. 64, no. 10, pp. 4457-4467, Oct. 2016, doi: 10.1109/TAP.2016.2598200.

[6] J.A. Diaz, D. Argiles, J.F. Monserrat and L. Rubio, "Characterization of the UWB Mobile Radio Channel Time Dispersion at 0.3 - 3GHz Band," in *Proc. 2006 3rd International Symposium on Wireless Communication Systems*, Valencia, 2006, pp. 149-153, doi: 10.1109/ISWCS.2006.4362277.

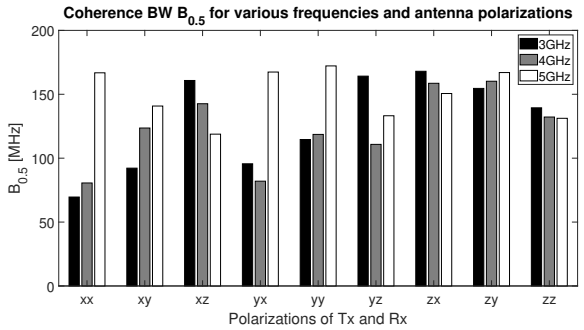

Fig. 13: Coherence Bandwidth $B_{0.5}$ for all frequency bands and all polarized pairs of Tx-Rx antennas

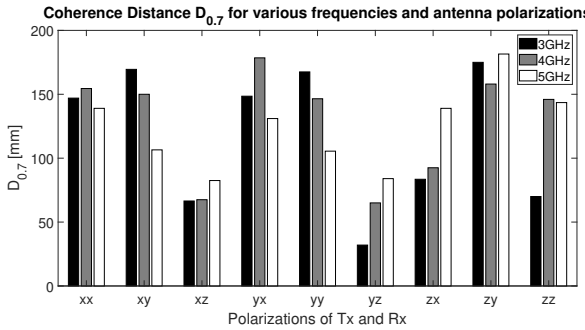

Fig. 15: Coherence distance $D_{0.7}$ for all frequency bands and all polarized pairs of Tx-Rx antennas

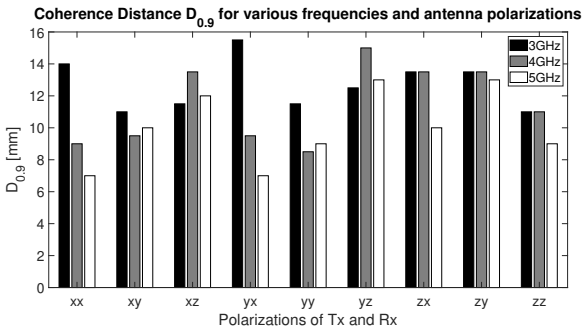

Fig. 14: Coherence distance $D_{0.9}$ for all frequency bands and all polarized pairs of Tx-Rx antennas

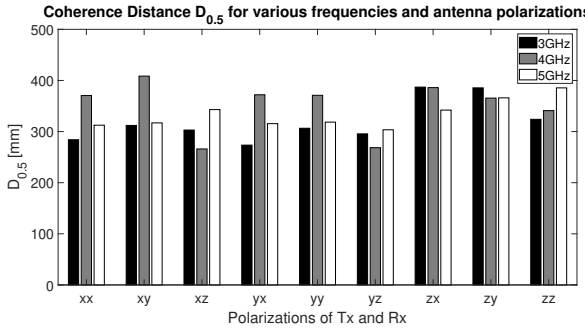

Fig. 16: Coherence distance $D_{0.5}$ for all frequency bands and all polarized pairs of Tx-Rx antennas

[7] Y. MIAO, *et al.*, "Investigating Correlation of Rough Surface Diffuse Scattering in Frequency Domain," in *Proc. 2019 13th European Conference on Antennas and Propagation (EuCAP)*, Krakow, Poland, 2019, pp. 1-3.

[8] J. Gutierrez-Meana, J.A. Martinez-Lorenzo and F. Las-Heras (July 5th 2011). High Frequency Techniques: the Physical Optics Approximation and the Modified Equivalent Current Approximation (MECA), Electromagnetic Waves Propagation in Complex Matter, Ahmed Kishk, IntechOpen, DOI: 10.5772/17307. Available from: https://www.intechopen.com/books/electromagnetic-waves-propagation-in-complex-matter/high-frequency-techniques-the-physical-optics-approximation-and-the-modified-equivalent-current-appr.

[9] Y. Miao, Q. Gueuning and C. Oestges, "Modeling the Phase Correlation of Effective Diffuse Scattering From Surfaces for Radio Propagation Prediction With Antennas at Refined Separation," in *IEEE Transactions on Antennas and Propagation*, vol. 66, no. 3, pp. 1427-1435, March 2018, doi: 10.1109/TAP.2018.2794372.

[10] N. Pinel, C. Bourlier, and J. Saillard, "Degree of Roughness of Rough Layers: Extensions of the Rayleigh Roughness Criterion and Some Applications," in *Progress In Electromagnetics Research B*, Vol. 19, 41-63, 2010. doi:10.2528/PIERB09110907.

[11] C.A. Balanis, in *Advanced engineering electromagnetics*, Hoboken: J. Wiley amp; Sons, 2012. pp, 341-346.

[12] F. Vico, et al., "Computational electromagnetics and fast physical optics," *Waves*, no. 1, pp. 155–161, Jan. 2009.

[13] M. Tlich , G. Avril, A. Zeddam (2008) Coherence Bandwidth and its Relationship with the RMS delay spread for PLC channels using Measurements up to 100 MHz. In: *Al Agha K., Carcelle X., Pujolle G. (eds) Home Networking. IFIP — The International Federation for Information Processing*, vol 256. Springer, Boston, MA.

[14] M.S. Varela and M.G. Sanchez, "RMS delay and coherence bandwidth measurements in indoor radio channels in the UHF band," in *IEEE Transactions on Vehicular Technology*, vol. 50, no. 2 , March 2001, pp. 515-525, doi: 10.1109/25.923063.

[15] J. Wagen, U.T. Virk and K. Haneda, "Measurements based specular reflection formulation for point cloud modelling," in *Proc. 2016 10th European Conference on Antennas and Propagation (EuCAP)*, Davos, 2016, pp. 1-5, doi: 10.1109/EuCAP.2016.7481727.

[16] M. Ahmad, *5G NR Standard and the Anatomy of a New Test Era*, IEEE Spectrum Accessed on: June 13, 2018. [Online]. Available: https://spectrum.ieee.org/telecom/internet/5g-nr-standard-and-the-anatomy-of-a-new-test-era.